Editors' Suggestion | Featured in Physics

Exploiting complex 3D-printed surface structures for portable quantum technologies

N. Cooper,[1,*] D. Johnson,[1] B. Hopton,[1] M. Overton,[1] D. Stupple,[2] A. Bratu,[2] E. Wilson,[2] J. Robinson,[2] L. Coles,[3] M. Papastavrou,[3] and L. Hackermueller[1]

[1] *School of Physics and Astronomy, University of Nottingham, University Park, Nottingham NG7 2RD, United Kingdom*

[2] *Torr Scientific Ltd., Pebsham Lane, Bexhill-on-Sea TN40 2RZ*

[3] *Metamorphic Additive Manufacturing Ltd, Riverside Chambers, Full Street, Derby, DE1 3AF, United Kingdom*

(Received 2 July 2025; revised 6 October 2025; accepted 10 November 2025; published 21 January 2026)

Portable quantum technologies require robust lightweight apparatus with superior performance. For techniques dependent upon high-vacuum environments, such as atom interferometers and atomic clocks, three-dimensional (3D) printing enables additional avenues to tailor in-vacuum gas propagation dynamics. We demonstrate intricate fine-scale surface patterning of 3D-printed vacuum components to increase the rate at which gas particles collide with the surface. By applying a nonevaporable getter coating for use as a surface pump, we show that the patterned surface pumps gas particles 3.8 times faster than equivalent flat areas. These patterns can be directly integrated into additively manufactured components, enabling application in close proximity to key experimental regions and contributing to overall mass reduction. We develop numerical simulations that show good agreement with this result and predict up to a tenfold increase in the pumping rate, for realistic surface structures. Our work has direct applications in enabling passively pumped portable quantum technologies but also establishes 3D printing as a powerful technique for the creation of optimized surface patterning to provide enhanced control over high-vacuum gas dynamics for a broad range of applications.

DOI: 10.1103/rg8y-rpsc

I. INTRODUCTION

A rapidly growing range of portable atom-based quantum technologies (QTs) are exploiting ultrahigh-vacuum (UHV) conditions to enable sensing and timing applications with unprecedented performance [1–7]. A significant challenge for field employment is to reduce the size, weight, and power consumption (SWAP) of vacuum equipment, especially pumps. While much progress in the miniaturization of experimental hardware such as optics [8–12], vacuum vessels [13,14], magnetic field generation [15], control electronics, [16] and integrated atom traps [17] has been demonstrated, vacuum pumps have developed more slowly and are now a major limiting factor. Solving this problem will facilitate the deployment of portable QTs for both industry and research. In addition to terrestrial QT applications, a range of exciting proposals to deploy space-based QTs [18] have been put forward for Earth monitoring [19,20], astronomical observations [21], and precision tests of fundamental physics [22–24]; low mass, power consumption, and heat dissipation are essential for such deployments. Understanding and exploiting the benefits offered by 3D-printed surfaces—in particular, in combination with 3D-printed chambers or hardware elements—can help overcome many of these challenges.

Passive pumping via nonevaporable getters (NEGs) [25–27] offers a promising route to unlock the full potential of portable QTs [28,29]. However, substantial increases in the pumping rate and pump capacity are required, particularly for some "problem" particle species with low pumping efficiency [30]. Solving this problem has the potential to greatly expand the scope and efficacy of portable QTs, even in applications where traditional vacuum technology is currently successfully employed. For example, the miniaturized magneto-optical trap operated aboard an unmanned aerial vehicle in Ref. [31] can be flown for only 18 min at a time, owing to the weight of the apparatus. The authors of Ref. [31] specifically identify superior passive pumping systems as a promising way to overcome this obstacle and increase utility. The portable quantum gravimeter described in Ref. [32] could

*Contact author: nathan.cooper@nottingham.ac.uk

Published by the American Physical Society under the terms of the Creative Commons Attribution 4.0 International license. Further distribution of this work must maintain attribution to the author(s) and the published article's title, journal citation, and DOI.

not currently be deployed in such a setting, as it has a total system mass in excess of 300 kg, which is substantially contributed to by vacuum and pumping apparatus. The space-based applications described above would benefit greatly from quantum sensors that could be deployed in small (one- or two-unit) CubeSat packages [33], but the size and weight limitations (0.001 m^3 and 2 kg per unit) currently prevent cold-atom-based quantum technologies from being thus deployed—we are not currently aware of any cold-atom sensor successfully deployed in a CubeSat package below six units [34].

By considering the physics of a diffuse gas interacting with a patterned surface, it is possible to engineer complex surfaces that enhance the performance of high-vacuum systems for QTs; specifically, we show that additive manufacturing (AM, also known as 3D printing) can create intricate surface structures that substantially increase the effectiveness of passive NEG pumps. Exploiting AM, these surfaces can be embedded directly within the walls of vacuum components, aiding compactness and facilitating integration into target systems. We demonstrate experimentally that appropriately structured parts of a 3D-printed NEG-coated surface can pump 3.8 times faster than equivalent flat regions.

We present numerical simulations, validated by our experimental results, which suggest up to a tenfold increase in the pumping speed with achievable surface geometries. The resulting improvement in the pumping rate through complex geometries can exceed the corresponding increase in total surface area. Furthermore, this enhancement can be realized without any increase in the projected surface area—which serves as a metric for the spatial footprint of the surface pump within the vacuum system. This approach to modeling the behavior of a rarefied gas interacting with complex surface patterning thus reveals optimal structures for NEG surface pumping, while also paving the way for AM-enabled surface texture engineering to be applied more broadly to meet the needs of emerging QTs in high-vacuum environments; this could include, e.g., the use of optimized surface patterns to control channel conductances, particle dwell times, or nozzle output distributions.

We produce AM surface structures in titanium alloy via additive manufacturing and they are confirmed as UHV compatible. Photographs of the surface structures tested are shown in Fig. 1(a) and their exact geometries are described below. Previous work has not only demonstrated AM of UHV components [35], but has also shown that AM allows conformal application of intricate structures over complex 3D surfaces [8,14]. Combined with the approach described herein, this establishes a clear pathway to integrated structured pumping surfaces, suitable to cover a large fraction of the internal surface area of a vacuum system, within nearly any UHV component (see Fig. 2). It may even be possible to design structured surfaces

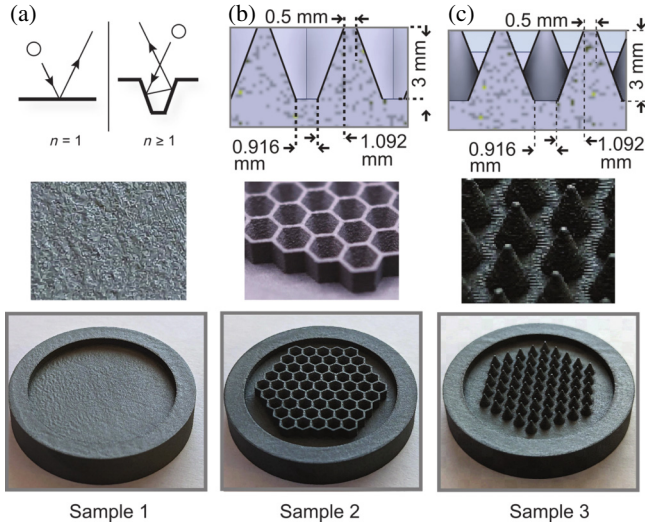


FIG. 1. The three-dimensionally (3D) printed surface structures experimentally tested for pumping performance, including a flat reference surface. (a) A diagram illustrating how tailored surface structures enable multiple collisions and photographs of the flat reference surface. (b) An array of tapered truncated hexagonal pockets. (c) A hexagonally packed array of conical protrusions.

that offer dual functionality, by simultaneously tailoring gas dynamics within the vacuum and exploiting structural optimization principles [36,37] to improve the strength-to-weight ratio or other relevant structural properties of the vacuum apparatus.

Beyond QTs, passive surface pumps play a role in maintaining UHV environments within a wide range of technologies and devices, from electron microscopy [38] and mass spectrometry [39] to prototype fusion reactors [40] and particle accelerators [41]. All such applications may benefit from improved pumping performance and the technology introduced here.

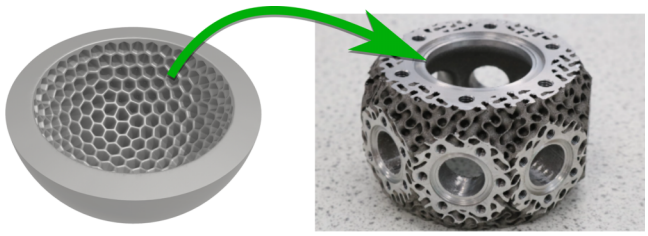


FIG. 2. An additively manufactured vacuum apparatus with internal surface structuring: the surface structures could be conformally mapped onto the interior surfaces of chambers and components. Herein, it is shown that, with an NEG coating applied to such a surface, this can enable large improvements in surface pump performance. Similar methods will likely enable tailored control of gas flow within high-vacuum apparatus. The AM chamber photographed here is described fully in Ref. [14].

II. THEORY AND SIMULATIONS

Monte Carlo simulation methods, based on ballistic particle propagation in the long mean-free-path limit, have been used to model the interactions of incident gas particles with structured surfaces. This approach allows rapid investigation of the properties of a wide range of surface structures, enabling optimization of surface patterns for specific applications. The employment of a Monte Carlo approach based on sequential simulation of individual particles makes the simulation process highly general; any surface pattern with a repeated unit cell can be simulated. The generality of the method facilitates analysis of complex surface geometries, allowing surface patterns to be engineered to forms optimal for specific applications.

Here, we target the application of optimizing pumping performance for surfaces coated with NEG material. Small-scale surface patterning increases the surface area available and thus yields a corresponding increase in total pumping capacity. However, these structures can also increase the pumping rate by factors significantly larger than the increase in surface area. The pumping rate is limited by the finite probability for an incident gas particle to be absorbed, via either binding or embedding, upon collision with the surface. This probability, P_s, depends on the particle species and getter material, but often $P_s \ll 1$ [30].

Complex surface structures can enhance the pumping efficiency for any $P_s < 1$. To simulate particle interactions with complex surfaces, we have considered particles incident upon both a flat and a structured surface, as depicted in Fig. 1(a). A particle incident upon the flat surface impacts the surface only once, yielding overall pumping probability P_s. However, a particle incident upon the structured surface, if not bound by the first collision, has a chance to reimpact the surface *before* passing back through the virtual surface marking the top-plane of the surface structure and can undergo multiple collisions in this way. This yields an effective pumping probability $P_e > P_s$.

To enable evaluation of P_e, we define $n \geq 1$ as the number of surface collisions that would be undergone by an incident nonsticking particle with $P_s = 0$. The effective pumping probability P_e for a real particle, with $P_s \neq 0$, is then given by

$$(P_e|n) = 1 - (1 - P_s)^n. \tag{1}$$

In the limit of $P_s \ll 1$, $(P_e|n)$ is equal to nP_s and thus $P_e = \langle n \rangle P_s$, resulting in an upper limit on the value of P_e for real particles, with $\langle n \rangle$ representing the maximum factor of improvement offered by the surface patterning.

Appropriate surface structures thus enable an increased pumping rate within the same projected area. Labeling the probability that a particle with $P_s = 0$ undergoes n collisions as $P(n)$, we can combine the probability distribution for $P(n)$ with (1) to obtain P_e for any value of P_s:

$$P_e = \sum_{n=1}^{\infty} (P_e|n) P(n). \tag{2}$$

However, obtaining $P(n)$ is nontrivial and depends on the surface geometry. To do this, we have developed a Monte Carlo simulation that models particle incidence upon the structured surface and particle propagation within the structured surface. Particles are sampled randomly from an isotropic background gas and propagated, in the long mean-free-path limit appropriate to high-vacuum environments, until they return through the top plane.

By default, we model reemission of particles that impact the surface using the standard cosine law [42], but we also consider isotropic reemission into the available half-space and find similar results [see Fig. 3(b)]. AM build processes create surface roughness on a scale that is small compared to the intentional feature size but large compared to the length scale of an atom or molecule. In the context of scattering from structured surfaces, this manifests as a partial randomization of the local surface orientation during particle emission, leading to increasingly isotropic emission. By considering the two extreme cases—a pure cosine distribution and fully isotropic emission—we establish bounds within which the actual system performance is expected to fall.

Particles are propagated in this way until they reemerge from the top plane of the surface. The number of collisions is then recorded and, by averaging over large numbers of particles [10^5 particles per data point for the data shown in Fig. 3(b)], the probability distribution $P(n)$ can be numerically approximated from the results. Equation (2) can then be applied to determine the increase in capture probability for an incident particle and thus the factor by which the pumping rate is improved, P_e/P_s.

A. Simulation results

Simulations have first been conducted for the two surface geometries depicted in Fig. 1: an array of tapered truncated hexagonal pockets (structure, or sample, 2) and a hexagonally packed array of conical protrusions (structure, or sample, 3). The exact realized geometry of the printed structures is shown in the figure. In the case of structure 2, we simulate an idealized form in which the pockets are fully tessellated without interstitial flat regions on the top surface, as such regions occur in our sample only for historical and technical reasons. In Fig. 3(a), we depict the key parameters of the simulation, including the surface angle θ, which is measured between the inclined regions of the structured surface and the normal to the top plane of the surface. Other, more complex, forms have also been considered and simulated, as illustrated in Fig. 4.

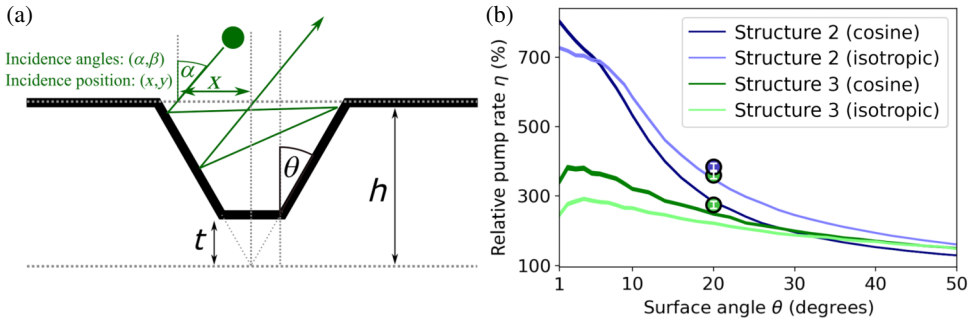


FIG. 3. (a) A sketch illustrating the key simulation parameters; the truncation ratio is given by t/h. (b) The effect of surface angle θ on the pumping efficiency, for $P_s \ll 1$, for both experimentally tested structures: hexagonal-pocket arrays (structure 2) and hexagonally packed cone arrays (structure 3). The simulations (blue lines for structure 2, green lines for structure 3), for either a cosine-law or isotropic scattering for reemission of particles from the surface, have employed 10^5 particles per point. The linewidth represents 1σ uncertainty bounds due to numerical error. Data points with error bars indicate experimental results for structure 2 (upper point, blue) and upper and lower bounds for structure 3 (middle and lower points, green). Pockets are assumed to be fully tesselated in structure 2.

Our simulations can predict the pumping-rate improvement expected for any finite value of P_s, but we display here the theoretically optimum case in which $P_s \ll 1$. This is a good approximation for many realistic situations [30] and is supported by our experimental results reported in the subsequent sections. This approximation inherently becomes a better estimate for the long-term pressure behavior of systems in which NEG surface pumping is the main pumping mechanism, since species with low P_s will tend to become the dominant constituents of the residual background gas.

The simulation results for the geometries in Fig. 1 are shown in Fig. 3(b). They indicate that large increases in the pumping speed are plausible using fine-scale surface texturing. For example, with $\theta = 10^\circ$ (an angle that remains plausible for sputter coating [43]), fully tesselated hexagonal pockets are predicted to enhance the pumping rate by a factor of between 5.3 and 5.9. They also show the strong dependence of the pumping efficiency on the surface angle θ. In Fig. 3, we show the results for either a standard cosine-law for reemission of particles from the surface or isotropic reemission into the available half-space. The circles indicate experimental data points for structure 2 (upper point, blue) and upper and lower bounds for structure 3 (middle and lower points, green). The simulations assume complete coverage of an infinite surface.

Simulation results for $\theta < 10^\circ$ indicate that the maximum pumping-rate increase achievable with these structures is around a factor of 8, achieved for surface angles $\lesssim 1^\circ$. This is relevant because certain printable materials—such as titanium—can function directly as getter materials when activated at sufficient temperature [44,45], potentially allowing for steeper surface angles in future applications.

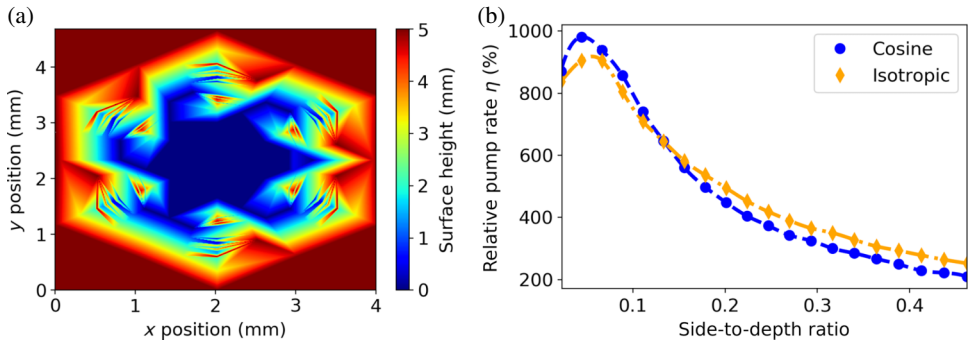


FIG. 4. (a) The height map of the intricately structured pocket with superior pumping performance. The total depth is set at 5 mm. (b) The simulated pumping-rate increase resulting from the structure displayed in (a) as a function of the ratio between the side length of the hexagon and the total pocket depth, when subject to a uniform stretch along the direction of the normal to the surface top plane. The numerical errors are smaller than the marker size. The dashed lines are cubic interpolations between data. Note that although a direct comparison with simpler geometries is not possible due to the absence of a clearly defined surface angle θ, the *maximum* pumping-rate improvement reaches a factor of 9 (10) for isotropic (cosine-distributed) reemission, exceeding the respective factors of 7 (8) found for polygonal-pocket forms.

In addition, a broad range of patterns have been simulated, the cross-section shape of which has been that of a regular polygon with between three and eight sides. The relative pumping-rate enhancement dependent on θ is similar for all these shapes, with only minor dependence on the number of sides of the polygon and the truncation parameter ($t/h \leq 0.2$). The results are given in the Supplemental Material [46].

Beyond simple polygonal forms, simulations do predict improvements in performance for some more complex forms. To demonstrate the ability of the simulations to tackle complex surfaces and almost arbitrary geometries, we have simulated the effect of intricate pocket shapes based upon geometry-inspired artwork ("Escher tilings"), one of which has been found to yield significant improvements in the pumping performance. This pocket shape is given by the height map shown in Fig. 4(a) and the corresponding maximum improvement in the pumping rate is shown in Fig. 4(b). Because the form simulated involves a range of different surface angles, it cannot be compared directly with the simpler polygonal-pocket forms for any specific surface angle. However, in this case the *maximum* possible pumping-rate improvement is considerably higher than that for simple polygonal-pocket forms, at a factor of 9 (10) for isotropic (cosine-distributed) scattering, respectively. This motivates further investigation of complex engineered surface patterns for enhancing QT devices and demonstrates the utility of these simulations in analyzing atom-surface interactions.

III. SAMPLE DESIGN AND FABRICATION

The small-scale surface structures have been parametrically designed using the computational tool GRASSHOPPER for RHINOCEROS 3D, enabling a scalable approach to the creation of tessellating features for enhanced passive pumping. Although this method has been initially applied to planar geometries, it has also been found that the method is capable of conformally integrating with more complex curved surfaces within larger components. This design methodology offers a versatile framework, ensuring that structured surfaces can be seamlessly applied to a wide range of geometrical configurations.

Hexagonal pockets (as recesses) and conical protrusions (as raised features) have been selected for exploration due to their efficient packing arrangements, which can easily be implemented in both planar and complex surfaces. The cone structure offers advantages in terms of outgassing and avoiding trapped gas pockets. For the hexagonal pattern, the interconnected nature of the hexagonal pockets enhances the structural integrity during printing: it therefore offers advantages in terms of printability, especially on overhanging features of larger components. Truncation of the structures has been employed to avoid build imperfections at sharp features; in the case of recessed features, this limits the potential for the formation of trapped gas pockets and thus ensures UHV performance.

AM enables the creation of sufficiently small and numerous features for compact integrated application within 3D-printed components (e.g., internal tubes, shields, or vacuum parts). Alternatively, it permits conformal application over complex internal surfaces of complete vacuum chambers (see Fig. 2) [14]. Note that the size of the build area on current metal-capable AM apparatus typically limits the size of any single part to approximately 30 cm in any one dimension, although of course multipart apparatus can be arbitrarily large. Additionally, for maximum efficacy and to recover the simulated situation above, the "main volume" of the vacuum apparatus must be large compared to the surface features—current AM capabilities limit the minimum feature size in Ti-6Al-4V Grade 5 to approximately 500 μm, meaning that chambers $\lesssim 1$ cm across will not fully benefit from surface structuring.

While various metals and UHV-compatible glass have been printed successfully [14,35,47], Ti-6Al-4V Grade 5 is particularly suitable for quantum technology applications, owing to its high strength-to-weight ratio and its relatively low electrical conductivity, which is important in mitigating eddy currents during atom-based sensing experiments. All experimental trials have therefore been conducted using Ti-6Al-4V Grade 5 and fabricated through laser powder-bed fusion. This method provides the necessary precision (< 100 μm resolution) and material properties to realize these designs at the required scale, demonstrating the suitability of additive manufacturing for the production of functional surfaces in advanced applications.

The AM fabrication process closely resembles that outlined in Ref. [14] and involves laser powder-bed fusion printing, followed by heat treatment and then optional surface treatments such as bead blasting. Following this a knife edge has been machined onto the vacuum flanges to enable attachment to UHV systems. Costs per sample (excluding NEG coating, which has been conducted by the authors) have been 150–200 GBP. These figures are typical for AM titanium components of this size at the time of writing. The lead times have been 2–4 weeks, dominated by administrative and work-flow constraints, with the actual physical processing time required on the order of 1–2 days. Conventional manufacturing of components with such surface structures would be extremely impractical and there is, therefore, no conventional equivalent. However, these costs are relatively small compared to the overall costs of a high-vacuum apparatus or compared to active pumping systems (which usually cost upward of 2000 GBP).

Following printing and postprocessing, the samples (the hexagonal-pocket array, the hexagonally packed cone array, and a flat reference sample) have been sputter coated with V-Zr-Ti NEG material. A composition range has been identified from the literature [48] that could be activated at

low temperatures around 200 °C, which is V 40% ± 20%, Zr 40% ± 20%, and Ti 20% ± 20% (all figures atomic % and all intervals absolute percentage points).

The sputter coating has been performed with a dual dc-magnetron system with one target of V-Zr and one of Ti-V composition, with both magnetrons running simultaneously at appropriate intensity to achieve the desired composition. The system has been calibrated to achieve a thickness close to 2 μm. Energy-dispersive x-ray (EDX) analysis has confirmed that the V, Zr, and Ti were present in acceptable proportions and that each element was well dispersed throughout the coating.

IV. EXPERIMENT AND RESULTS

The AM titanium samples have been produced as 47.9-mm-diameter disks so that, with a machined Conflat® knife edge, the samples could be incorporated into a standard DN40 rotatable vacuum flange and attached to corresponding vacuum ports. Samples with AM structures 1–3 have been produced (see Fig. 1) and NEG coated. An additional flat 3D-printed sample has also been manufactured for use as a control sample, without NEG coating. Due to initial concerns over potential build imperfections—ultimately revealed to be unnecessary by the quality of the resulting samples—a 500-μm flat space has been allowed between adjacent pockets in sample 2; this differs from the theoretical optimum version of structure 2 used for simulation purposes, but it is easy to reconcile the two by allowing for the flat-area fraction of the real array (see below).

Visual examination of all samples has revealed no significant build errors or distortions and the samples have been sputter coated with V-Zr-Ti getter material following the procedure outlined above. The entire interior surface of the AM flange, a total area of $A_R = 1134$ mm^2, has been coated with NEG material. The structured surface has been restricted to an approximately hexagonal region of total area $A_S = 726$ mm^2. Within the hexagonal-pocket array, flat areas of 500-μm width separate adjacent pockets, leaving a remaining $A_P = 508$ mm^2 of the area that actually corresponds to the interior of the pockets.

Initial pumping tests have been performed using a residual gas analyzer (RGA, Stanford Research Systems RGA100 with electron multiplier), connected to a test rig containing a pressure gauge (Arun Microelectronics AIG17G), a turbomolecular pump that could be isolated via an all-metal bonnet valve, and the sample under test. Standard baking and activation procedures have been applied (see the Supplemental Material [46]). The bonnet valve has then been closed and the changes in partial pressure for H_2, starting at the time of valving-off the turbomolecular pump, have been recorded by the RGA and are displayed in Fig. 5. Partial pressures for CO_2, N_2 and CO have been found to be negligible by comparison; data for this are shown in the Supplemental Material [46]. The

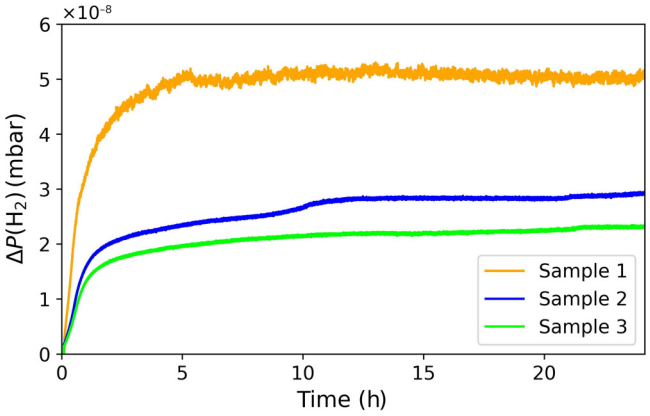


FIG. 5. The partial-pressure increase for H_2 from RGA tests after closing of the gate valve for three different samples. The initial partial pressures were $P_{H_2} = 1.9 \times 10^{-10}$ mbar for sample 1, $P_{H_2} = 1.2 \times 10^{-10}$ mbar for sample 2, and $P_{H_2} = 1.0 \times 10^{-10}$ mbar for sample 3.

results clearly confirm that the surface structures of samples 2 and 3 substantially decrease the observed pressure rise and that hydrogen, which has small P_s for the NEG coating used [30], is the dominant background gas species.

To quantitatively assess the increase in the pumping performance, tests have been conducted using the apparatus shown in Fig. 6(a). The chamber, with an internal volume of 0.20 l, has been evacuated and baked, and the NEG coating activated as described in the Supplemental Material [46]. The angle valve seen in Fig. 6(a) has then been closed and the pressure as a function of time monitored using the pressure gauge (Pfeiffer IKR 270 Compact Cold Cathode Gauge). An initial pressure spike occurred due to the disturbance caused by physically closing the valve. This has been followed in each case by a gradual decline in the measured pressure. The raw data are shown in Fig. 6(b). A small decrease in pressure has also been observed for an uncoated sample [gray line in Fig. 6(b)]. This can most likely be explained by contamination of the system with NEG material from previous tests or by a pumping contribution from the ion gauge. Furthermore, a sudden pressure drop occurs for all samples at a consistent pressure of approximately 4×10^{-7} mbar, corresponding to a change in the operating mode of the pressure gauge that significantly alters its pumping and outgassing contributions. By performing a differential measurement, comparing structured NEG-coated samples to a flat NEG-coated sample, the influence of all such sources of spurious pumping or outgassing can be negated.

In order to determine a pumping-rate coefficient γ (see Eq. (3) below) under comparable conditions, each data set has been truncated at the point at which the measured pressure reached 10^{-5} mbar during the decline following the initial spike; this has ensured repeatable and consistent starting conditions. The rate of pressure decrease, dp/dt, has then been determined in each case as a function of

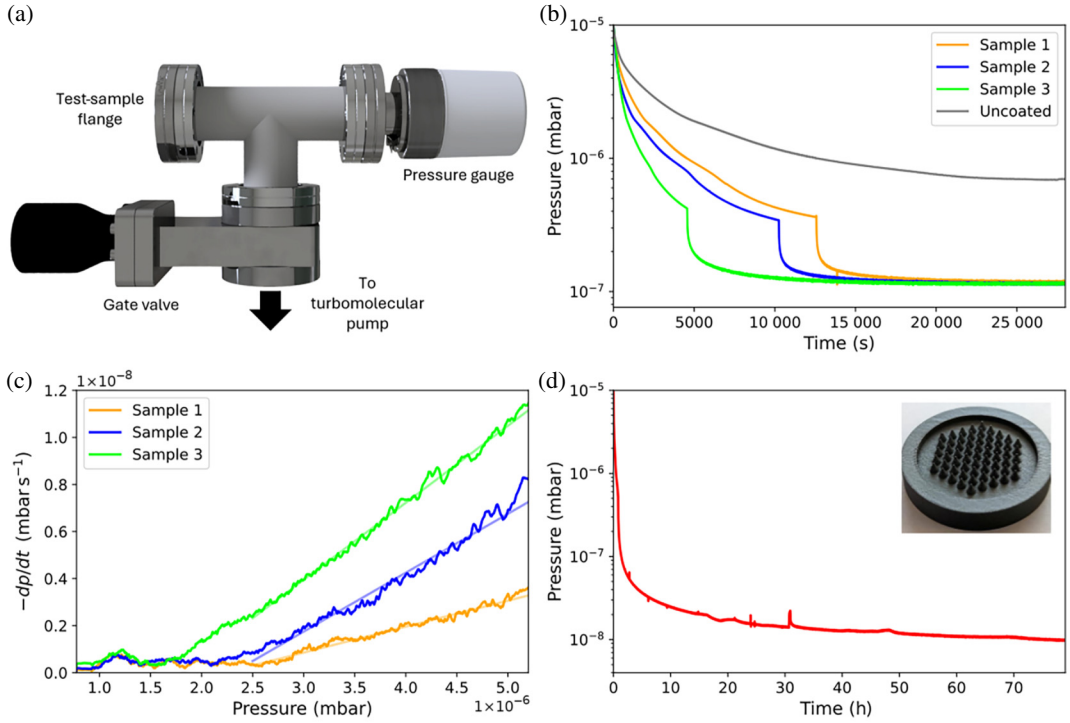


FIG. 6. (a) The setup used to test the pumping performance of the additively manufactured and NEG-coated structured samples. The closure of the gate valve allows pumping rates to be inferred from pressure data recorded by the vacuum gauge. (b) The measured chamber pressure against time for each test sample, including a printed uncoated sample. (c) The net pumping rates $-dp/dt$ for each NEG-coated sample as a function of pressure. Linear fits have been used to calculate the pumping-rate coefficients for the pumped volume, which are $\gamma_1 = 1.10(2) \times 10^{-3}\,\mathrm{s}^{-1}$, $\gamma_2 = 2.50(3) \times 10^{-3}\,\mathrm{s}^{-1}$, and $\gamma_3 = 3.27(3) \times 10^{-3}\,\mathrm{s}^{-1}$. (d) The long-term pressure data for sample 3 (pictured), showing that the pumping performance is maintained over > 3 days and a final pressure of 9.7×10^{-9} mbar is reached.

pressure, using linear interpolation, where necessary, to enable a consistent set of data points across all samples. To eliminate the influence of spurious pumping and/or contamination sources, the rate of the pressure drop for the uncoated sample has been subtracted.

The residual rate of the pressure drop attributable to the NEG coating has then been plotted against pressure in each case [see Fig. 6(c)]. The net rate of the pressure drop under constant pumping conditions is given by

$$\frac{dp}{dt} = C - \gamma p, \tag{3}$$

where C is a constant rate of pressure increase resulting from leaks and outgassing, p is the current pressure in the system, and γ is the pumping-rate coefficient, which represents the "strength of pumping" [49,50]. In Fig. 6(c), $-dp/dt$ is plotted against p and the gradient corresponds to the pumping-rate coefficient γ_i for each sample. The ratio of the fitted gradients for the different samples therefore gives the ratio of their pumping-rate coefficients.

The results are summarized in Table I and show that sample 3 offers an NEG-based pumping-rate coefficient greater than that of sample 1 by a factor of $\gamma_3/\gamma_1 = 3.0 \pm 0.1$, while structure 2 increases it by a factor of $\gamma_2/\gamma_1 = 2.3 \pm 0.1$.

In order to quantify the improvement introduced by the 3D-printed geometry and to compare to simulations, a useful measure is the pumping-rate coefficient per unit projected area of the structured surface, denoted $\gamma_{i,s}$ for sample i. To calculate $\gamma_{i,s}$, allowance must be made for the flat parts of the sample, as well as for the fact that particles

TABLE I. A comparison of the experimentally tested samples: the "Relative surface area," which refers to the relative total surface area per unit projected area of the structured surface; the measured pumping-rate-coefficient enhancement γ_i/γ_1 for each sample flange; and the corresponding relative pumping-rate coefficient per unit structured area, $\eta_i = \gamma_{i,s}/\gamma_{1,s}$, for each sample. Sample 2*, together with the related η_2^* inferred from the measured γ_2, represents the theoretical optimum form of sample 2 without interstitial flat regions.

AM sample	Relative surface area	γ_i/γ_1	η_i
1	1	1	1
2	2.3	2.3(1)	3.0(1)
2*	2.9	...	3.8(1)*
3	1.9	3.0(1)	2.7(1) (min.) 3.6(1) (max.)

can enter through the vertical sides of the array in structure 3 (see the Supplemental Material [46]). This second consideration results in the determination of upper and lower bounds to $\gamma_{3,s}$, depending on what assumptions are made about pumping by the sides of the array.

These calculations yield the enhancement factors, $\eta_i = \gamma_{i,s}/\gamma_{1,s}$, of the pumping-rate coefficient per unit area, given by $\eta_2 = 3.0 \pm 0.1$, and the upper and lower limits of $\eta_{3,\max} = 3.6 \pm 0.1$ and $\eta_{3,\min} = 2.7 \pm 0.1$ for structures 2 and 3, respectively. These factors of improvement show that the method offers substantial benefits even with relatively conservative surface designs. It is interesting to note that η exceeds the ratio by which the total surface area is increased.

For the purposes of comparison with simulation, η_{2^*}—the improvement in the pumping-rate coefficient per unit projected area for the hexagonal pockets themselves, excluding the interstitial flat regions—is found to be 3.8 ± 0.1. The results are displayed in Fig. 3 and include both bounds for structure 3.

Simulation and experiment show good correspondence, with the experimental data displaying a slightly larger pumping rate enhancement than expected. This can be explained by the influence of small-scale surface roughness caused by the AM build process, which has not been included in the simulation.

Overall, the experimental results confirm the basic premise of our theory and show that it provides a good description of the actual pumping performance. In particular, our simulations are suitable estimates to predict the performance of AM surface structures of known geometry. This further supports the simulation results shown in Figs. 3 and 4, which indicate that much larger improvements in the pumping performance are possible. For example, Fig. 4 predicts $7.5 < \eta < 8$ for pockets of the form shown with a side-to-depth ratio of 0.1; given that standard laser powder-bed fusion manufacturing offers a resolution < 100 μm, this can be achieved with absolute pocket depths of a few millimeters. At the optimal side-to-depth ratio of 0.028, the simulations predict $9.1 < \eta < 9.8$ for this pocket shape.

In Fig. 6(d), we show longer-term pressure data taken with sample 3, indicating that this sample can pump a volume of 0.20 l for > 70 h of operation to a pressure $< 10^{-8}$ mbar. As no degradation of performance has been observed within the window of observation, these data provide only a lower limit on pump longevity, which may in fact be far longer. In general, the increase in total surface area when applying an NEG coating to a structured surface, rather than a flat one, increases the total pump capacity and thus extends operational longevity.

V. CONCLUSIONS

We have demonstrated that additively manufactured complex surface structures can be employed to manipulate gases in ultrahigh-vacuum chambers. In particular, we have shown that structures 3D printed in ^{64}Ti are UHV compatible and enable a tailored enhancement in the number of surface-scattering events induced by the structured elements. Outgassing tests (see the Supplemental Material [46]) have not measured any adverse effects of the AM build process on vacuum performance. Applications include controlling particle-propagation pathways and dwell times in UHV devices and high-efficiency surface pumping. Experimentally, we have shown a factor-of-3.8 increase in the pumping rate per unit area by adding a purpose-designed surface texture to an NEG-coated surface. We have developed and presented Monte Carlo simulations that enable prediction of the performance of complex AM surface geometries. Comparing theory and experiment, we have found good agreement, while the experimental results have slightly exceeded the predictions of the Monte Carlo simulations. These simulations reveal a range of interesting surface structures that offer even greater improvements in pumping rate, predicting up to a tenfold increase in the pumping rate for some more complex forms.

Promising directions for further development include adapting the technique to provide optimum performance from components that control gas flow via impact with a surface, such as collimation nozzles [51,52] and cold plates [53]. Conformal application over a large fraction of the interior surface of a vacuum system, coupled to direct activation of the titanium build material as an NEG pump, is also a very interesting avenue of future research, with the potential to enable extreme pumping performance and underpin portable UHV and even extreme-high-vacuum (XHV) systems.

The capabilities provided by such engineered AM surface structures are relevant to numerous technologies and devices across QTs and beyond. QT applications will include next-generation portable gravimeters [54,55], cold-atom magnetometers [56,57], atomic clocks [58,59], and quantum accelerometers [60]. Application areas outside QTs include mass spectrometers [39], particle accelerators [61], and electron microscopes, especially where the use of methods such as environmental transmission electron microscopy or the study of novel materials imposes additional pumping and gas-flow requirements [62,63]. The passive nature of such surfaces and the ease with which AM can shape components for integration into compact lightweight systems makes this approach ideally suited to field-deployable [64] or space-based [65] devices.

ACKNOWLEDGEMENTS

This work has been supported by the UK Engineering and Physical Sciences Research Council (EPSRC) (Grants No. EP/T001046/1, No. EP/R024111/1, No. EP/Y005139/1, and No. EP/Z533166/1), the Innovate UK

projects Quantum Atom-based Positioning for Train Control with a Hybrid Accelerometer (QAPTCHA) (Grant No. 10143484) and Quantum Technologies Enabled by Additive Manufacturing (QTEAM) (Grant No. 10031462), the John Templeton Foundation (Grant No. 62420), and the EPSRC Impact Acceleration Account (Grant No. EP/X525765/1).

D.J. and B.H., with assistance from N.C., collected the pumping data used for quantitative determination of the pumping rates of the samples. B.H. with assistance from D.J. and N.C., analyzed the resulting experimental data. N.C. developed and performed the numerical simulations. D.S., E.W., and J.R. performed nonevaporable getter coating of the samples and outgassing measurements, and collected species-specific pumping data using the residual gas analyzer. L.C. and M.P. developed the computational design methodology and applied it to enable sample printing. A.B., L.C., and L.H. managed the project and supervised the work. N.C. and L.H. conceived the idea of the project. N.C., D.J., B.H., M.O., D.S., L.C., and L.H. wrote the paper.

DATA AVAILABILITY

The data that support the findings of this paper are not publicly available. The data are available from the authors upon reasonable request.

[1] V. Menoret, P. Vermeulen, N. Le Moigne, S. Bonvalot, P. Bouyer, A. Landragin, and B. Desruelle, Gravity measurements below 10^{-9} g with a transportable absolute quantum gravimeter, Sci. Rep. **8**, 12300 (2018).

[2] Y. Bidel, O. Carraz, R. Charriere, M. Cadoret, N. Zahzam, and A. Bresson, Compact cold atom gravimeter for field applications, Appl. Phys. Lett. **102**, 144107 (2013).

[3] M. E. Limes, E. L Foley, T. W. Kornack, S. Caliga, S. McBride, A. Braun, W. Lee, V. G. Lucivero, and M. V. Romalis, Portable magnetometry for detection of biomagnetism in ambient environments, Phys. Rev. Appl. **14**, 011002(R) (2020).

[4] X.-B. Deng, Y.-Y. Xu, X.-C. Duan, and Z.-K. Hu, Precisely mapping the absolute magnetic field in vacuum by an optical Ramsey atom interferometer, Phys. Rev. Appl. **15**, 054062 (2021).

[5] Y. B. Kale, A. Singh, M. Gellesch, J. M. Jones, D. Morris, M. Aldous, K. Bongs, and Y. Singh, Field deployable atomics package for an optical lattice clock, Quantum Sci. Tech. **7**, 045004 (2022).

[6] K. W. Martin, G. Phelps, N. D. Lemke, M. S. Bigelow, B. Stuhl, M. Wojcik, M. Holt, I. Coddington, M. W. Bishop, and J. H. Burke, Compact optical atomic clock based on a two-photon transition in rubidium, Phys. Rev. Appl. **9**, 014019 (2018).

[7] B. Tennstedt, N. Weddig, and S. Schön, Improved inertial navigation with cold atom interferometry, Gyroscopy Navig. **12**, 294 (2021).

[8] S. Madkhaly, L. Coles, C. Morley, C. Colquhoun, M. Fromhold, N. Cooper, and L. Hackermüller, Performance-optimized components for quantum technologies via additive manufacturing, PRX Quantum **2**, 030326 (2021).

[9] S. Madkhaly, N. Cooper, L. Coles, and L. Hackermüller, High-performance, additively-manufactured atomic spectroscopy apparatus for portable quantum technologies, Opt. Express **30**, 25753 (2022).

[10] A. Strangfeld, B. Wiegand, J. Kluge, M. Schoch, and M. Krutzik, Compact plug and play optical frequency reference device based on Doppler-free spectroscopy of rubidium vapor, Opt. Express **30**, 12039 (2022).

[11] S. Dyer, K. Gallacher, U. Hawley, A. Bregazzi, P. F. Griffin, A. S. Arnold, D. J. Paul, E. Riis, and J. P. McGilligan, Chip-scale packages for a tunable wavelength reference and laser cooling platform, Phys. Rev. Appl. **19**, 044015 (2023).

[12] F. Wang, N. Cooper, Y. He, B. Hopton, D. Johnson, P. Zhao, C. J. Tuck, R. Hague, T. M. Fromhold, R. D. Wildman, L. Turyanska, and L. Hackermüller, Additive manufacturing of functionalised atomic vapour cells for next-generation quantum technologies, Quantum Sci. Tech. **10**, 015019 (2024).

[13] K. Weng, B. Wu, J. Lin, Y. Zhou, B. Cheng, and Q. Lin, Compact magneto-optical trap with a quartz vacuum chamber for miniature gravimeters, J. Opt. Soc. Am. B **37**, 1637 (2020).

[14] N. Cooper, L. Coles, S. Everton, I. Maskery, R. Campion, S. Madkhaly, C. Morley, J. O'Shea, W. Evans, R. Saint, P. Krüger, F. Oručević, C. Tuck, R. Wildman, T. Fromhold, and L. Hackermüller, Additively manufactured ultra-high vacuum chamber for portable quantum technologies, Addit. Manuf. **40**, 101898 (2021).

[15] R. Saint, W. Evans, Y. Zhou, T. Barrett, T. M. Fromhold, E. Saleh, I. Maskery, C. Tuck, R. Wildman, F. Oručević, and P. Krüger, 3D-printed components for quantum devices, Sci. Rep. **8**, 8368 (2018).

[16] P. Ruksasakchai, C. E. Cowdell, L. Sanchez, M. Weyland, and M. F. Andersen, A microcontroller based self-locking laser system, Rev. Sci. Instrum. **93**, 043008 (2022).

[17] L. Chen, C.-J. Huang, X.-B. Xu, Y.-C. Zhang, D.-Q. Ma, Z.-T. Lu, Z.-B. Wang, G.-J. Chen, J.-Z. Zhang, H. X. Tang, C.-H. Dong, W. Liu, G.-Y. Xiang, G.-C. Guo, and C.-L. Zou, Planar-integrated magneto-optical trap, Phys. Rev. Appl. **17**, 034031 (2022).

[18] A. Belenchia, M. Carlesso, O. Bayraktar, D. Dequal, I. Derkach, G. Gasbarri, W. Herr, Y. L. Li, M. Rademacher, J. Sidhu, D. K. Oi, S. T. Seidel, R. Kaltenbaek, C. Marquardt, H. Ulbricht, V. C. Usenko, L. Wörner, A. Xuereb, M. Paternostro, and A. Bassi, Quantum physics in space, Phys. Reports **951**, 1 (2022).

[19] F. Migliaccio, M. Reguzzoni, K. Batsukh, G. M. Tino, G. Rosi, F. Sorrentino, C. Braitenberg, T. Pivetta, D. F. Barbolla, and S. Zoffoli, MOCASS: A satellite mission concept using cold atom interferometry for measuring the Earth gravity field, Surv. Geophys. **40**, 1029 (2019).

[20] R. Haagmans, C. Siemes, L. Massotti, O. Carraz, and P. Silvestrin, ESA's next-generation gravity mission concepts, Rend. Fis. Acc. Lincei **31**, 15 (2020).

[21] F. Müller, O. Carraz, P. Visser, and O. Witasse, Cold atom gravimetry for planetary missions, Planet. Space Sci. **194**, 105110 (2020).

[22] M. He *et al.*, The space cold atom interferometer for testing the equivalence principle in the China space station, Npj Microgravity **9**, 58 (2023).

[23] F. Sorrentino *et al.*, A compact atom interferometer for future space missions, Microgravity Sci. Technol. **22**, 551 (2010).

[24] L. Badurina *et al.*, AION: An atom interferometer observatory and network, J. Cosmol. Astropart. Phys. **2020**, 011 (2020).

[25] E. Sartori, M. Siragusa, P. Sonato, F. Siviero, M. Mura, E. Maccallini, A. Ferrara, P. Manini, S. Hanke, and C. Day, Development of nonevaporable getter pumps for large hydrogen throughput and capacity in high vacuum regimes, Vacuum **214**, 112198 (2023).

[26] Y. Li, D. Hess, R. Kersevan, and N. Mistry, Design and pumping characteristics of a compact titanium-vanadium non-evaporable getter pump, J. Vacuum Sci. Tech. A **16**, 1139 (1998).

[27] H. Kodama, S. Ohno, M. Tanaka, M. Tanaka, K. K. Okudaira, K. Mase, and T. Kikuchi, Low-cost, high-performance nonevaporable getter pumps using nonevaporable getter pills, J. Vacuum Sci. Tech A **34**, 051601 (2016).

[28] R. Boudot, J. P. McGilligan, K. R. Moore, V. Maurice, G. D. Martinez, A. Hansen, E. de Clercq, and J. Kitching, Enhanced observation time of magneto-optical traps using micro-machined non-evaporable getter pumps, Sci. Rep. **10**, 16590 (2020).

[29] B. J. Little, G. W. Hoth, J. Christensen, C. Walker, D. J. De Smet, G. W. Biedermann, J. Lee, and P. D. Schwindt, A passively pumped vacuum package sustaining cold atoms for more than 200 days, AVS Quantum Sci. **3**, 035001 (2021).

[30] O. Seify, O. B. Malyshev, R. Širvinskaitė, R. Valizadeh, and A. Hannah, Optimisation of the RGA location in the evaluation of NEG coating pumping properties, Vacuum **165**, 207 (2019).

[31] L. Earl, J. Vovrosh, M. Wright, D. Roberts, J. Winch, M. Perea-Ortiz, A. Lamb, F. Hayati, P. Griffin, N. Metje, K. Bongs, and M. Holynski, Demonstration of a compact magneto-optical trap on an unstaffed aerial vehicle, Atoms **10**, 32 (2022).

[32] B. Stray *et al.*, Quantum sensing for gravity cartography, Nature **602**, 590 (2022).

[33] https://www.esa.int/Enabling_Support/Preparing_for_the_Future/Discovery_and_Preparation/CubeSats European space agency: CubeSats, accessed September 12, 2025.

[34] D. Devani *et al.*, Gravity sensing: Cold atom trap onboard a 6U CubeSat, CEAS Space J **12**, 539 (2020).

[35] J. Vovrosh, G. Voulazeris, P. G. Petrov, J. Zou, Y. Gaber, L. Benn, D. Woolger, M. M. Attallah, V. Boyer, K. Bongs, and M. Holynski, Additive manufacturing of magnetic shielding and ultra-high vacuum flange for cold atom sensors, Sci. Rep. **8**, 2023 (2018).

[36] J. Plocher and A. Panesar, Review on design and structural optimisation in additive manufacturing: Towards next-generation lightweight structures, Mater. Des. **183**, 108164 (2019).

[37] C. Pan, Y. Han, and J. Lu, Design and optimization of lattice structures: A review, Appl. Sci. **10**, 6374 (2020).

[38] Q. Zhang, M. Tanaka, M. Takeguchi, and K. Furuya, Analytical UHV transmission electron microscopy studies of electronic structure changes between as-deposited Mn and Mn silicide on Si(111) surface, Surface Sci. **507-510**, 453 (2002).

[39] W. Zhang, X. Xia, Y. Zhang, T. Peng, and Q. Yang, A novel sample preparation method for ultra-high vacuum (UHV) secondary ion mass spectrometry (SIMS) analysis, J. Anal. At. Spectrom. **33**, 1559 (2018).

[40] E. Sartori, M. Siragusa, G. Berton, C. Cavallini, S. Dal Bello, M. Fadone, L. Grando, D. Marcuzzi, D. Rizzetto, G. Serianni, P. Sonato, M. Zaupa, F. Dinh, A. Ferrara, E. Maccallini, M. Mura, F. Siviero, and V. Toigo, Design of a large nonevaporable getter pump for the full size ITER beam source prototype, J. Vacuum Sci. Tech. B **41**, 034202 (2023).

[41] C. Benvenuti, A new pumping approach for the large electron positron collider (LEP), Nuclear Instr. Methods Phys. Res. **205**, 391 (1983).

[42] J. Greenwood, The correct and incorrect generation of a cosine distribution of scattered particles for Monte-Carlo modelling of vacuum systems, Vacuum **67**, 217 (2002).

[43] W. Zhou, J. Brock, M. Khan, and K. Eid, Oblique angle deposition-induced anisotropy in Co_2FeAl films, J. Magn. Magn. Mater. **456**, 353 (2018).

[44] J. Kamiya, K. Takano, K. Wada, and H. Yuza, Some methods of making titanium vacuum chamber act as getter pump for UHV/XHV, Joint Accelerator Conferences Website (JACoW) **IPAC2021**, WEPAB337 (2021).

[45] J. Kamiya, K. Takano, H. Yuza, and K. Wada, Evaluation of titanium vacuum chamber as getter pump, e-J. Surf. Sci. Nanotechnol. **20**, 107 (2022).

[46] See the Supplemental Material at http://link.aps.org/supplemental/10.1103/rg8y-rpsc for additional simulation results, vacuum compatibility and residual gas analysis testing of printed samples, full technical details of simulation procedures, vacuum baking, and NEG activation, as well as detailed explanation of the calculation of $\gamma_{i,s}$.

[47] F. Wang, N. Cooper, D. Johnson, B. Hopton, A. Murray, R. McMullen, T. M. Fromhold, R. Hague, L. Turyanska, and L. Hackermüller, Additive manufacturing for advanced quantum technologies, Adv. Quantum Technol. **8**, e00186 (2025).

[48] A. Prodromides, C. Scheuerlein, and M. Taborelli, Lowering the activation temperature of TiZrV non-evaporable getter films, Vacuum **60**, 35 (2001).

[49] L. Detian, C. Yongjun, F. Yan, X. Zhenhua, and Z. Lan, Very low gas flow measurements for UHV/XHV and leak calibration, Metrologia **50**, 15 (2012).

[50] L. Peksa, T. Gronych, M. Jerab, P. Repa, M. Vicar, Z. Krajicek, D. Prazak, F. Stanek, and J. Tesar, Dynamic extension—a new principle for a vacuum primary standard for UHV-range (10^6 $--$ -10^{10} Pa) calibration of hot cathode ionisation gauges, Vacuum **85**, 1047 (2011).

[51] N. Cooper, E. Da Ros, J. Nute, D. Baldolini, P. Jouve, L. Hackermüller, and M. Langer, Collimated dual species oven source and its characterisation via spatially resolved fluorescence spectroscopy, J. Phys. D: Appl. Phys. **51**, 105602 (2018).

[52] R. Hahn, T. Battard, O. Boucher, Y. J. Picard, H. Lignier, D. Comparat, N.-A. Keriel, C. Lopez, E. Oswald, M. Reveillard, and M. Viteau, Comparative analysis of recirculating and collimating cesium ovens, Rev. Sci. Instrum. **93**, 043302 (2022).

[53] E. W. Streed, A. P. Chikkatur, T. L. Gustavson, M. Boyd, Y. Torii, D. Schneble, G. K. Campbell, D. E. Pritchard, and W. Ketterle, Large atom number Bose-Einstein condensate machines, Rev. Sci. Instrum. **77**, 023106 (2006).

[54] C.-Y. Li, J.-B. Long, M.-Q. Huang, B. Chen, Y.-M. Yang, X. Jiang, C.-F. Xiang, Z.-L. Ma, D.-Q. He, L.-K. Chen, and S. Chen, Continuous gravity measurement with a portable atom gravimeter, Phys. Rev. A **108**, 032811 (2023).

[55] T. Zhang, L.-L. Chen, Y.-B. Shu, W.-J. Xu, Y. Cheng, Q. Luo, Z.-K. Hu, and M.-K. Zhou, Ultrahigh-sensitivity Bragg atom gravimeter and its application in testing Lorentz violation, Phys. Rev. Appl. **20**, 014067 (2023).

[56] A. Fregosi, C. Gabbanini, S. Gozzini, L. Lenci, C. Marinelli, and A. Fioretti, Magnetic induction imaging with a cold-atom radio frequency magnetometer, Appl. Phys. Lett. **117**, 144102 (2020).

[57] Hamish A. M. Taylor, C. C. Bounds, A. Tritt, and L. D. Turner, Unambiguous measurement in an unshielded microscale magnetometer with sensitivity below 1 $\mathrm{pT}/\sqrt{\mathrm{Hz}}$, Phys. Rev. Appl. **22**, 024047 (2024).

[58] J. Grotti *et al.*, Geodesy and metrology with a transportable optical clock, Nat. Phys. **14**, 437 (2018).

[59] Q. Hao, S. Yang, J. Ruan, P. Yun, and S. Zhang, Integrated pulsed optically pumped Rb atomic clock with frequency stability of 10^{-15}, Phys. Rev. Appl. **21**, 024003 (2024).

[60] F. Narducci, A. Black, and J. Burke, Advances toward fieldable atom interferometers, Adv. Phys.: X **7**, 1946426 (2022).

[61] H. Hähnel and U. Ratzinger, First 3D printed IH-type linac structure—proof-of-concept for additive manufacturing of linac RF cavities, Instruments **6**, 9 (2022).

[62] R. Yang, L. Mei, Y. Fan, Q. Zhang, H.-G. Liao, J. Yang, J. Li, and Z. Zeng, Fabrication of liquid cell for in situ transmission electron microscopy of electrochemical processes, Nat. Protoc. **18**, 555 (2023).

[63] Y. Lin, M. Zhou, X. Tai, H. Li, X. Han, and J. Yu, Analytical transmission electron microscopy for emerging advanced materials, Matter **4**, 2309 (2021).

[64] S. E. Crawford, R. A. Shugayev, H. P. Paudel, P. Lu, M. Syamlal, P. R. Ohodnicki, B. Chorpening, R. Gentry, and Y. Duan, Quantum sensing for energy applications: Review and perspective, Adv. Quantum Technol. **4**, 2100049 (2021).

[65] R. Kaltenbaek, A. Acin, L. Bacsardi, P. Bianco, P. Bouyer, E. Diamanti, C. Marquardt, Y. Omar, V. Pruneri, E. Rasel, B. Sang, S. Seidel, H. Ulbricht, R. Ursin, P. Villoresi, M. van den Bossche, W. von Klitzing, H. Zbinden, M. Paternostro, and A. Bassi, Quantum technologies in space, Exp. Astron. **51**, 1677 (2021).